Mining, Metallurgy & Exploration
https://doi.org/10.1007/s42461-026-01497-0

Coal Bursting at the Elk Creek Mine: A Western United States Case Study

M Shawn Boltz[1] · Derrick JA Chambers[1] · Mark K Larson[1] · Heather E Lawson[1] · Wille Törnman[2]

Received: 20 August 2025 / Accepted: 3 February 2026

Abstract
Coal bursts pose a substantial threat to operations and mine workers. The coal mines in the North Fork Valley (NFV) in the United States (US) have experienced many coal bursts, often with distinct characteristics from those of other US coal mining regions. Seismic monitoring in conjunction with other in-mine instrumentation was conducted at the Elk Creek Mine in the NFV during the mining of four longwall panels. Nearly one million seismic events with magnitudes ranging between −2.0 and 3.1 were detected, of which approximately 200,000 located within the study region surrounding the extracted panels with 80 m location errors. Five events were coal bursts that resulted in injury or significant in-mine damage. This study examines the characteristics of the recorded seismicity, focusing on the largest magnitude coal burst. The moment tensor solution for the largest event corroborates the findings of other studies that faulting contributed to the damaging seismicity at the mine. Anomalous ground conditions, abnormal caving behavior, and the migration of seismic events characterized a latent seismic hazard that later resulted in a large coal burst. Moreover, the observed load transfer distance at the mine is significantly greater than what is suggested using common empirical design methods, which are largely based on coal mines in the Eastern US. This case study provides an example of the utility of seismic data at a burst-prone underground coal mine. The Elk Creek dataset, which is co-published with this study, is a valuable resource for future mine safety research.

Keywords Coal mining · Longwall mining · Seismicity · Coal burst · Mine stability · Instrumentation

1 Introduction

Underground coal mines can experience a wide variety of dynamic failures which pose substantial threats to operations and mine workers. Despite decades of research, these events remain poorly understood and difficult to manage. Due to differences in definitions and time ranges, the number of reported coal bursts varies. Zhang et al. [1] report approximately 3,000 bursts from several countries, including the United States (US), China, Poland, Germany, and the Czech Republic over multiple time ranges spanning the last century. Kidybiński [2] estimates that more than 30,000 gas-pressure-driven dynamic failure events, known as outbursts, have occurred globally since 1843 and describes these events as "the most dangerous natural phenomenon" impacting mine worker safety. In the US, the Mine Safety and Health Administration (MSHA) maintains a database of incidents that includes 429 discrete coal dynamic failures occurring in the United States between 1945 and the first half of 2020 that meet the criteria for reporting [3]. Rong [4] reports that at least 100 fatalities and 1,000 injuries have occurred in the approximately 200 Chinese coal mines which experienced dynamic failures in the past decade. The Upper Silesian Coal Basin, which is shared between Poland and the Czech Republic, has experienced hundreds of dynamic failures [5], and many other countries with coal mines including Germany, Japan, Australia, and Russia, have reported similar events [6].

Efforts to categorize coal dynamic failures date back at least to mid-1930s when Rice [7] made a distinction between events that tend to colocate with damage (pressure bursts) and events which occur some distance from the damage observed in the workings (shock bursts). Iannacchione

✉ M Shawn Boltz
mboltz@cdc.gov

1 Spokane Mining Research Division, National Institute for Occupational Safety and Health, Spokane, WA, USA

2 RockSigma, Luleå, Sweden

Published online: 03 March 2026

[8] defined three types of coal bursts based on the associated mechanism: excessive stress, seismic shock, and loss of confinement. Taking a slightly different approach, Vardar et al. [9] classified events based on the primary energy source driving the failure. Their categories include strain energy stored in the coal seam (bursts), strain energy in surrounding strata (bumps), or gas pressure in the coal (outbursts). Frith et al. [10] illustrated these burst categories as a Venn diagram, with overlapping circles to indicate the potential for multiple event energy sources. They further divided bursts into fault-driven failures and compressive failures of competent units. The diversity of these taxonomies demonstrates the complex and eclectic nature of dynamic failures in coal mines, as well as a pervasive inconsistency in nomenclature. For the sake of simplicity, but at the cost of precision, this work simply refers to any damaging seismic event in a coal mine as a coal burst.

The deep coal mines of the Western United States have experienced a wide variety of coal bursts. Those experienced by the coal mines in the state of Utah, which account for over half of recent coal bursts in US coal mines [11], demonstrate the wide range in event magnitude, location, mechanics, and damage. The most severe event since the turn of the century is the Crandall Canyon Mine disaster in 2007 in which six miners and three rescue workers were killed. A regional seismic network registered the event at a magnitude of 3.9 and waveforms were consistent with convergence of mine workings [12]. Observations made by rescue workers indicated wide-scale coal pillar failure while the mine roof remained largely intact [13]. There are also cases of larger events minimally impacting mine workers. In 2000, a thick sandstone unit failed in the overburden of a Utah longwall mine resulting in a magnitude 4.2 event. While the event triggered a rock slide on the surface that caused some damage to a road and railroad track above the mine, there was little in-mine damage and no injuries [14]. The experience of another Utah mine demonstrates that even low-magnitude events can result in injuries and fatalities when workers are near the seismic source. In this case, two fatalities and several injuries resulted from relatively small (magnitude < 2) events occurring on the mining face between 1998 and 2006 [15].

While coal bursts in the state of Utah are largely related to stored energy in the coal or near-seam strata, the experience in Colorado mines is more varied. The Mid-Continent mines, for example, experienced severe gas-driven outbursts, which is rare for US coal mines [16]. Coal bursts in the mines of the Somerset Coal Field, situated in Colorado's North Fork Valley (NFV), often occurred in areas with only moderate strength roof and floor, some distance from the highest stressed zones, and are more associated with geological structure rather than near-seam thick competent strata. There were also multiple cases of damaging events occurring in development sections, the mechanics of which remain "enigmatic" [17]. The events of the NFV were so severe, they prompted the installation and operation of a local seismic network [18], an uncommon practice for US coal mines.

This work details the extensive efforts conducted by the National Institute for Occupational Safety and Health (NIOSH) and the Oxbow Mining Company to study the coal bursts occurring in the Elk Creek Mine, a deep longwall mine in the NFV, from the years 2009 to 2013. During this time, several significant coal bursts severely disrupted the operation. A concise narrative, description of seismicity, and analysis of the largest coal burst is offered. Additionally, details about the jointly published dataset are given. The dataset includes mine maps and extraction sequences; seismic data from a microseismic system consisting of both in-mine and surface stations; qualitive ratings of rib, roof, and floor conditions; near-seam core; data from borehole pressure cells (BPCs); and several others. This extensive dataset represents a unique resource on which future studies can build to better understand and manage coal bursts.

2 Geology and Mine History

The NFV is situated in central Colorado, adjacent to Highway 133. The Somerset Coal Field contains six primary coal seams, which are part of the Mesaverde Formation. Only three of the seams, locally referred to as the B, D and E seams, are commercially viable. The regional structural dip is 3° to 5° to the north-northeast. The strata exhibit regularly spaced, near-vertical jointing, with the predominant joints having an average orientation of N76°E and secondary jointing oriented N18°W [19]. The study area is intersected by several steeply dipping faults striking N80°−90°E with minimal offset.

Figure 1 shows the generalized stratigraphy of the region. Roof lithologies tend to cycle between near-shore and marine deposits as a function of the area's proximity to the Cretaceous Western Interior Seaway at the time of deposition, resulting in rapid transitions between sandstones, siltstones, mudstones, occasional rider seams and bone coal stringers through the immediate mine roof [20, 21]. Seam thickness is variable, ranging from approximately 3 m to more than 6 m in minable seams. At the Elk Creek Mine, coal was extracted from the upper D seam with a mining height of 3.0–3.4 m, leaving coal in the floor in areas where the coal seam is thicker. Localized thermal metamorphism as the result of proximity to igneous intrusions, referred to as "burn zones", exist in some of the mines operating in the NFV and appear to increase dynamic failure behavior.

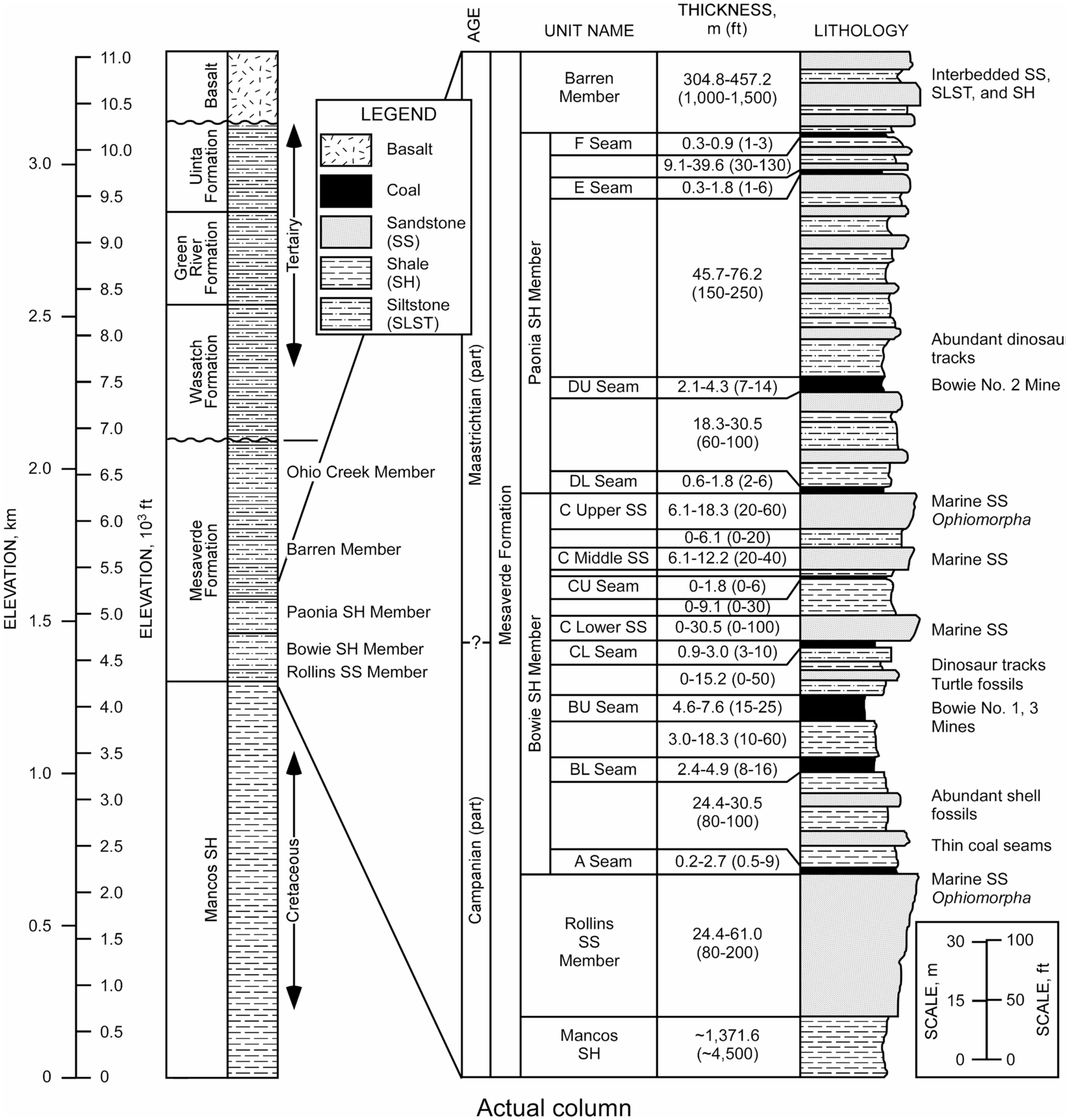

Fig. 1 Stratigraphy of the NFV from Larson et al. [22]. The Elk Creek Mine extracted coal from the upper D seam (DU Seam).

However, these zones are spatially limited with no regional effects.

Agapito et al. [23] summarized stress measurements of others by overcoring borehole deformation gauges at mines in the NFV. The average principal horizontal stress is oriented roughly N 81° E with a maximum to minimum horizontal stress ratio of 3.7, although there is significant variability, likely due to the influence of topography and other structural features [23, 24].

The Elk Creek mine began development in 2002 and extracted coal from the upper D seam. During the study period (November 2009 to January 2013), four panels were mined in the northeast part of the mine as shown in Fig. 2. The gateroads are incremented from South to North.

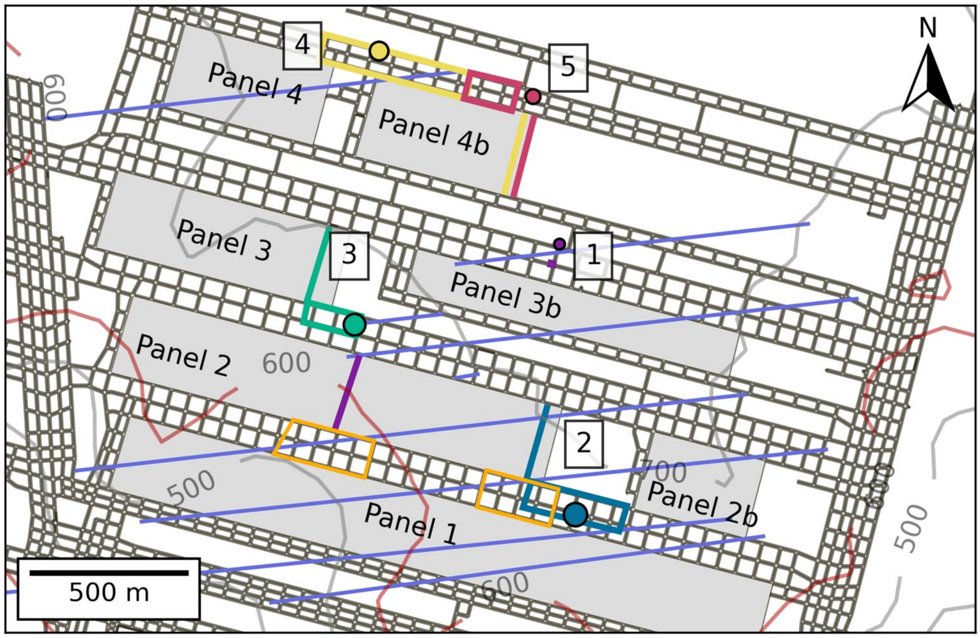

Fig. 2 Mine map. The contours show overburden in meters. Faults are shown as light purple lines. Circles denote coal burst events and are colored the same as their corresponding damage areas and face positions, denoted by rectangles and solid lines, respectively. The orange rectangles indicate "anomalous" zones on the 2 N gateroad. Mined out regions are shaded grey. Panels were mined from northwest to southeast, but development occurred from southeast to northwest

For example, the tailgate of Panel 1 is 1N and the gateroad between Panels 1 and 2 is referred to as 2N. Panel widths and pillar sizes are summarized in Table 1. The mine employed a three-entry system, and the entries are similarly incremented from South to North. The topographic relief around the mine is highly variable and during the time of the study, extraction depths varied from approximately 500 m to 700 m.

The immediate roof was highly variable but generally consisted of siltstone interlaced with weak layers of shale and coal. Some areas had meandering sandstone channels. The floor was composed of coal and a fireclay of variable thickness that acted as a split between the upper and lower D seam. This split widened to the northeast, such that the immediate floor composition in the 1 N gateroad was approximately 3 m of coal, shifting to about 1 m of fireclay underlain by coal and occasional siltstone stringers in 2 N. The coal seam was divided into four distinct depositional layers, separated by both depositional horizons and changes in macrolithotype. Coal cleat was moderately to poorly developed, dependent upon depositional layer. Upper layers tended toward bright banded coal and consequently were more well-cleated, while the lowermost quarter of the mined portion of the seam was dull and more friable with poorly developed to absent cleating. It is in this lowermost depositional layer where the most mining-related damage was observed.

2.1 Anomalous Deterioration Zones

Several anomalous zones spanning multiple pillars were observed in the 1 N and 2 N gateroads (the anomalous zones in the 2 N gateroad are denoted as orange rectangles in Fig. 2). These zones experienced markedly worse deterioration compared to the rest of the gateroads, even during development. The development of these zones appeared to be influenced by local geology as they exhibited a notable shift in both cleat spacing and direction. Rather than the regular, blocky character typically observed, the face cleat in these areas occurred as tightly spaced "swarms" oriented N 67 E [25]. Photographs of the conditions in 2 N are shown in Fig. 3. While floor heave wasn't commonly observed in 1 N, it was observed ahead of the longwall face starting early in the panel for 2 N, even under normal conditions, as seen in Fig. 3a. The roof of 2 N was largely intact under normal conditions. However, in the anomalous zones, the floor heave and roof deterioration progressed much more quickly than under normal conditions. Both anomalous zones in 2 N are intersected by faults, but not every fault-gateroad intersection resulted in an anomalous zone. Additionally, no faulting was apparent for the anomalous zones in 1 N [26].

Table 1 Panel and pillar dimensions

Panel Name	Panel Width	Pillar Dimensions	Inter-Panel Barrier Width
Panel 1	236 m	58 m by 61 m centers	–
Panel 2	236 m	58 m by 73 m centers	–
Panel 2b	236 m	58 m by 73 m centers	–
Panel 3	236 m	58 m by 73 m centers	–
Panel 3b	142 m	33 m by 73 m centers	75 m
Panel 4	236 m	33 m by 73 m centers	75 m
Panel 4b	236 m	33 m by 73 m centers	75 m

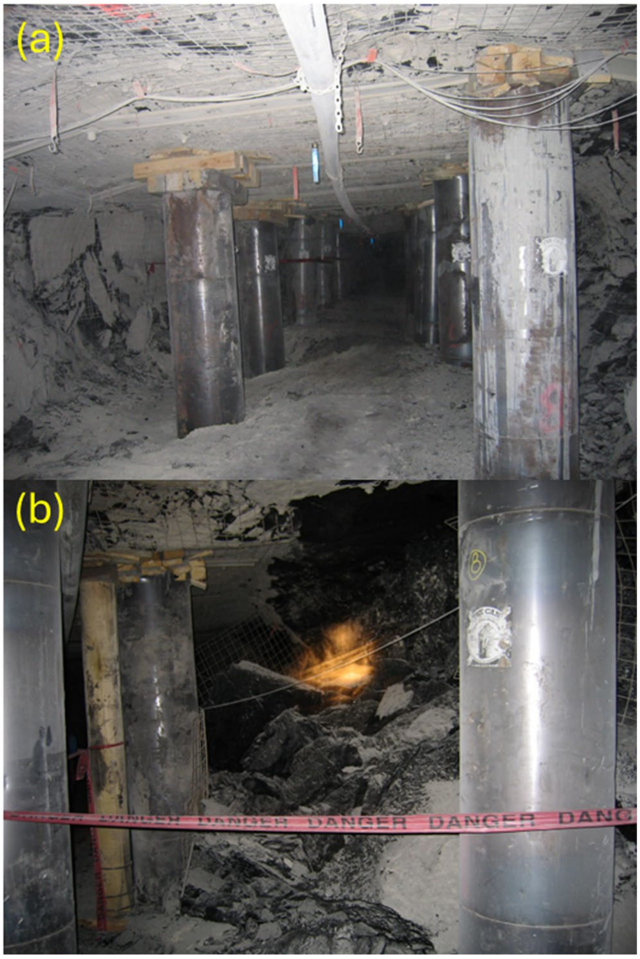

Fig. 3 Photos of the ground conditions in the 2 N gateroad during mining of Panel 2 showing (**a**) normal conditions with floor heave and (**b**) typical damage in the anomalous zone

2.2 Coal Bursts

Five significant coal bursts occurred during the mining of Panels 2–4. These events, as well as the narrative provided by the Mine Safety and Health Administration (MSHA), are listed in Table 2 and indicated on Fig. 2. One of these events, Event 1, occurred in response to gateroad development, while the others occurred during longwall retreat. After Event 2, which damaged a 3-hectare area of pillars in Panel 2's tailgate [11], the longwall was advanced 300 m ahead to bypass the damaged area and the remainder of the panel was extracted (labeled Panel 2b in Fig. 2). Mining in Panel 3 started shortly afterward and progressed for 700 m before another large burst, Event 3. This event occurred just ahead of the face in the 3 N gateroad, damaging a 1.6-hectare area of tailgate pillars [11]. Mining was stopped and a sub-panel (Panel 3b) was developed, leaving a 75-m-wide interpanel barrier, with a row of yield pillars, between Panel 2 and Panel 3b to provide additional isolation from the abutment load of Panel 2. Panel 3b was extracted without issue. A 75-m-wide interpanel barrier was similarly introduced between Panels 3 and 4, with a row of yield pillars separating the barrier from Panel 4. Panel 4 also had a small 140 m barrier built into the panel about 500 m outby of the panel start to avoid mining through a sandstone channel that crossed the coal seam. Event 4 occurred in 5 N after mining

Table 2 Listing of damaging burst events

Event	Date (Local time, YYYY-MM-DD HH: MM: SS)	M[a]	MSHA Description (edited for brevity)	Location
1	2010-12-03 17:37:10	1.5	Coal rib bump occurred after the miner operator had graded to the face and bumped into the coal face. The operator was standing outby the miner tail when he was hit by coal from behind the screened rib.	Development (Headgate of Panel 3)
2	2011-02-17 15:47:20	3.1	Not in database.	Tailgate of Panel 2
3	2011-10-18 23:24:16	3.0	A non-injury mountain bump[b] occurred longwall tailgate entries. From the longwall face outby for 60 feet in the #3 entry between 28 and 29 x-cut and inby 28 x-cut in the #2 entry.	Tailgate of Panel 3
4	2012-12-02 11:44:37	2.7[c]	Mountain bump around 25 crosscut, [along] sand channel of the [Panel 4b] start line. This resulted in floor hiccup and rib falls [from] crosscut 20 to 26 in the #2 and #3 entries.	Headgate of Panel 4
5	2013-01-02 03:11:58	2.3	A non-injury mountain bump occurred inby the longwall. Additional floor heave and rib falls. Some damage to ventilation controls, outby to x-cut 19 #2 and #3 entries. Same area as Event 4.	Headgate of Panel 4

[a]Local magnitude, see Eq. (1)

[b]Mountain bump" is an historical term sometimes used in the US to describe a coal burst

[c]The United States Geological Survey reported a local (Richter) magnitude of 3.4 for this event https://earthquake.usgs.gov/earthquakes/eventpage/usp000jwc5/executive

approximately 470 m of Panel 4b and the damage spanned a 4-hectare area stretching back to the within-panel barrier. A final event (Event 5) occurred a month later in the same area. The mine was abandoned shortly afterwards due to the initiation of an underground fire.

3 Data and Methods

A variety of data were collected during the study, including a seismic event catalog, measurements of pressure changes in the coal seam with BPCs, measurements of load and closure of instrumented support Cans, measurements of roof-to-floor entry closures, roof sag determined by multipoint extensometers and sonic probes [26]. The locations of the different instrumentation sites and seismic stations are shown in Fig. 4. The seismic stations were located on the surface and in the mine. The other geotechnical data were collected at or near four instrumentation sites: 1 N Inby (A), 1 N Outby (B), 2 N Inby (C) and 2 N Outby (D), and identified in Fig. 4. Figure 5 shows a timeline of mining, seismic monitoring, and data collection at each instrumentation site.

Ground condition surveys were conducted in parts of the 1 N gateroad and in entries 2 and 3 of the 2 N gateroad to track changing conditions. These surveys followed the rating criteria developed by Lawson et al. [27]. Also included in the dataset are longwall face positions as a function of time and some photographs of conditions and the instrumentation. For the first two panels, precise longwall positions were extracted from production reports, and for the remainder of the study they were linearly extrapolated from monthly positions included in the mine map. Additional details are provided in the following subsections.

3.1 Seismic Catalog Creation

Seismic monitoring efforts in the NFV began in 2007 to assess the possibility of mining-induced seismicity damaging local reservoirs. At that time, a small number of temporary surface sensors were deployed that lacked real-time telemetry. In collaboration with the Bowie and West Elk mines, the seismic network later expanded to include 10 surface stations, and the focus of the network shifted to managing and studying mining-induced events [18]. These surface stations typically consisted of a three-component strong-motion accelerometer and 1-Hz vertical geophone. Starting in late 2009, a network of “close-in” stations was installed at the Elk Creek mine, illustrated in Fig. 4, using a seismic monitoring system manufactured by Integrated Seismic Systems International (ISS, now the Institute of Mine Seismology or IMS). The data from the close-in stations

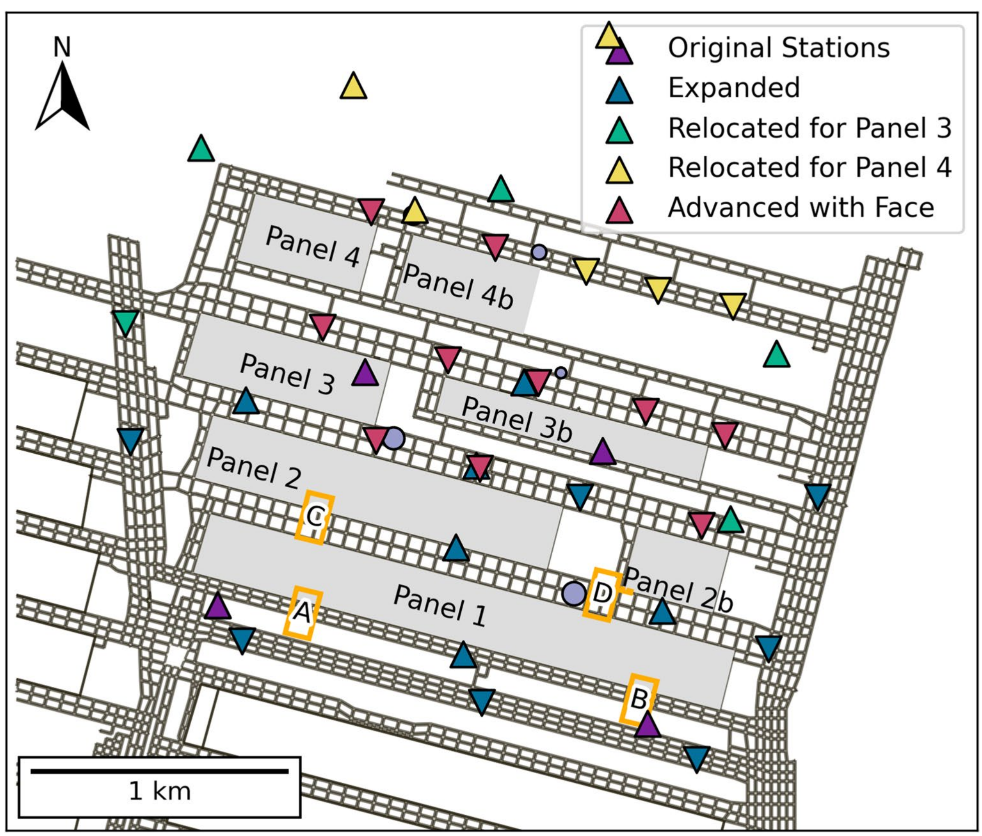

Fig. 4 Map of seismic stations and instrumentation sites in relation to the mine workings. Surface stations are represented by upright triangles, while inverted triangles denote underground stations. The station symbols are colored according to installation date. Orange rectangles delineate in-mine instrumentation sites and purple circles denote the locations of the significant events

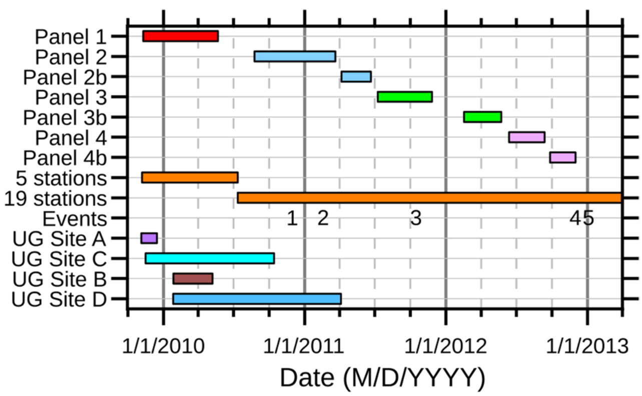

Fig. 5 Timeline showing the timing of extraction of the different longwall panels, data collection periods for seismic monitoring and other underground instrumuntation, and the timing of significant coal burst events (with event numbering matching Table 2)

initially consisted of four surface sites, each of which had a three-component geophone (labeled as "Original Stations" on Fig. 4). One of the sites also had a colocated shallow borehole sensor. The network was expanded in mid-2010 to include an additional six surface sites and eight underground sites (labeled "Expanded" on Fig. 4) for a total of 19 sensors. The underground stations consisted of three-component geophones installed in shallow boreholes drilled into the roof from mine level. The sensors were periodically relocated as mining advanced to maintain good azimuthal coverage around the longwall face, including two sensors that were routinely moved with face advance. There were only 19 sensors operating at a given time, but each time a sensor was moved it was assigned a new identifier, resulting in 39 unique station names and locations over the lifetime of the system. The sampling rates for the in-mine stations and surface stations were 5,000 Hz and 1,000 Hz, respectively. Because the network was frequently reconfigured, its sensitivity and event location accuracy varied with time.

The Elk Creek microseismic data were recorded on triggered mode, meaning digital waveforms were saved only when a trigger threshold was exceeded. Furthermore, waveforms from the Elk Creek network were only archived when a trigger was successfully associated to an event. An analysis for other mines suggests that these associated waveforms correspond to only about 15% of the total triggered data [28]. Although this substantially reduced the total data volume, it resulted in potentially losing valid events. Additionally, many files did not contain sufficient pre-trigger data. On the underground stations, in particular, the P-wave arrival was often excluded due to a poor arrival time estimate resulting from a low signal-to-noise ratio for the P wave. Because of the short pre-event time configured in the system, this often resulted in the exclusion of the P phase in the waveform file. Consequently, the data for the underground stations were only included in a relatively small percentage of event files.

Table 3 Velocity model used for event locations

Layer	*P*-Wave Velocity (m/s)	S-Wave Velocity (m/s)
Upper	2,771	1,600
Lower	3,801	2,195

Table 4 Interface between the two velocity model layers

Component	South	West	Down
Reference Point (mine coordinates, m)	−5,002	−11,001	−1,831
Upwards Normal	−0.0644	−0.0267	−0.9976

An initial seismic catalog was created with ISS's JMTS software. Event locations were determined using a homogeneous velocity model with a P-wave velocity of 3,048 m/s and S-wave velocity of 2,042 m/s. King [29] later created a model consisting of two layers over a half space. The velocities of the two layers are described in Table 3 and the interface between the two layers is described in Table 4. The data were reprocessed in 2024 using RockSigma's Bayesian Estimator for Mining-Induced Seismicity (BEMIS) [28]. BEMIS uses a self-calibrating approach [28] to account for heterogeneities within the rock mass. The velocity calibration initially used the King [29] model as a starting point. This calibration method enables both temporal and spatial updates to the velocity structure, providing more precise event locations than a static model (see, e.g., Törnman et al. [30]). This improvement shows tighter clustering of events around the mine workings compared to the ISS system. Events that occurred during the mining of Panel 1, when the network consisted of only four stations, were excluded from BEMIS processing due to the insufficient number of stations for reliable calibration.

BEMIS estimates radiated seismic energy in the time domain, while seismic moments are calculated using the method described by Törnman et al. [31], based on the Brune model [32] with a Q-value of 30. Both approaches account for noise and include spatiotemporal compensation for attenuation (see Törnman and Martinsson [28] for more details). The local magnitude calculation is based on the seismic moment (M_0, N-m) and radiated energy (E, J):

$$M_L = 0.272\log_{10}E + 0.392\log_{10}M_0 - 4.63 \tag{1}$$

The BEMIS-processed events are the preferred source of information in the catalog with supplements from the original ISS catalog to fill two gaps: (1) before the installation of the full network, and (2) during a 7-hour gap on December 2, 2012, between 00:00 and 07:00 UTC where the events were inadvertently skipped due to an error in the batch processing using BEMIS. For all subsequent processing, only events with a location error of 80 m for the BEMIS-processed events and 30 m for the ISS catalog events were used. The location procedure described in Törnman and Martinsson [28] reduces location uncertainty relative to a static model, as shown in Törnman et al. [30]. However, the primary distinction in location uncertainty threshold between the two approaches lies in how the location uncertainty is estimated. BEMIS estimates the size of the credible region of the hypocenter distribution, whereas ISS determines location uncertainty solely from travel-time residuals, hence not including deficiencies in the system layout and generally underestimating the true uncertainties. For instance, when the system layout is nearly linear, as shown in Törnman et al. (2024, Fig. 2), the resulting uncertainty forms a donut-shaped region. Although this region covers a large area, all credible coordinates within it will have small travel-time residuals, resulting in often unrealistic but smaller uncertainties in general. Event 1 had a location error of 114 m, higher than the cutoff, so it was explicitly added back into the catalog. Finally, events outside of the study area, as defined in Table 5, are excluded.

3.2 Geotechnical Instrumentation and Load Transfer Distance

Various measurements, including pressure changes from BPCs, support loads in the Cans, closure measurements, and ground condition surveys were used to determine the load transfer distance (LTD), or the maximum distance ahead of the face at which mining-induced stress can be detected [26]. Details of the installed instrumentation and methods for estimating LTD can be found in NIOSH [26]. The sensitivities of the LTD determinations were method dependent. Using BPCs was the most sensitive, followed by using instrumented support Cans. Using ground condition surveys to determine this distance was useful in this regard, but this method was about 40% less sensitive than using BPCs to sense the first indication of mining-induced stress increase.

The BPCs and support Cans were located in the gateroads or panel ahead of the longwall face and not at the side of the panel. Therefore, the maximum distances ahead of the face at which a mining-induced stress increase occurred were converted to equivalent LTDs. This was accomplished using a plot of stress-change contours calculated with a displacement discontinuity model, Mulsim [33], calibrated for conditions of this dataset.

Load transfer distance is important because it can be used to calibrate the stiffness of strata in numerical models. For LaModel, Heasley recommends calibrating the rock mass stiffness using the distance from the side of the panel within which 90% of the mining-induced vertical stress increase is transferred [38]. Considering measurement sensitivity and repeatability, a consistent increase in cell pressure of 140 kPa as measured with BPCs was used as a threshold to determine 90% transfer distance [26, 39]. The sensitivity of detection increase was adjusted similarly for support Cans and ground condition surveys. The relative distance sensitivities were determined, with BPCs being the most sensitive [40].

Table 5 Study volume extents (in mine coordinates)

Direction	Minimum (m)	Maximum (m)
East	9,800	12,800
North	4,200	6,500
Vertical	1,400	2,100

4 Results

4.1 Seismic Observations

The catalog consists of a total of 983,379 mining-induced events and 4,033 noise triggers and false positives. After excluding events that did not meet the location or location error criteria, the catalog contained 197,779 events. The criteria used to distinguish mining-induced events from noise triggers are strongly linked to location uncertainty and can vary substantially between manual processors as shown in Appendix A in Törnman and Martinsson [28]. Therefore, a substantial portion of the events with higher location errors were likely mis-classified noise triggers. Figure 6 shows histograms of the local magnitudes both before and after applying quality filtering. Events above magnitude 3.1 (the magnitude of the largest coal burst) in the pre-filtered dataset were inspected and found to be artefacts. After filtering, the local magnitudes range from − 2 to 3.1, with a magnitude of completeness around −0.5. There are 78 events with magnitude ≥ 2.

As mentioned in Sect. 3.1, events with a location error > 80 m were excluded from analysis. Most of the location error is in the vertical direction, as seen by the uncertainty planes plotted in Fig. 7. This is due to the preferential use of the surface array (e.g., Boltz et al. [41]) and inconsistent inclusion of data from the in-mine stations. As a result, it is not possible to determine whether the events are originating at, above, or below the coal seam, though most of the events clearly originate near the coal seam.

The locations of the events are plotted in plan view in Fig. 8a. Most of the seismicity locates on the face and in the gateroads of the active panel. Events continue to occur in the gateroads of previous panels due to loading from the expansion of the gob (mined out region). The clusters of events on the mains to the south of Panel 1 occurring during mining of Panels 3–4 are likely data processing artefacts as the clusters are approximately co-located with seismic sensors.

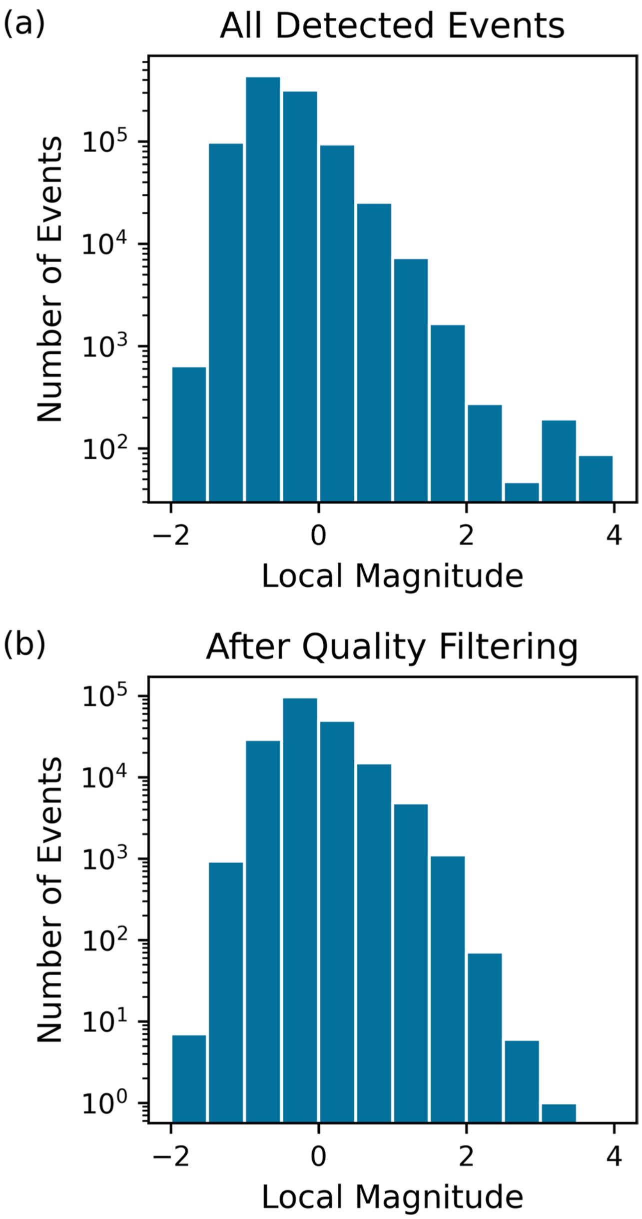

Fig. 6 Histogram of local magnitudes (**a**) before applying quality filtering and (**b**) after applying filtering

It is often insightful to visualize coal mine seismicity in a face-centered view since most events occur near the active mining face. Figure 8b shows event locations relative to the face at the time of each event. Most of the events locate near or ahead of the face, though it is important to note that the interpolated face position typically lags slightly behind the true face position. In addition to events across the face, events also locate along the gateroads stretching back into the gob, consistent with the gateroad pillars taking the abutment load and yielding as mining progresses. There is a small cluster of events that occurred on the headgate of Panel 1 (purple) that occurred notably ahead of the face. These events occur in the approximate location of Event 2, which took place during mining of the next panel. There is also a small cluster of magnitude 2 + events that occur on the face in this same area. Most of the magnitude 2 + events that occurred were either on the face or on the tailgate side of the panel. The cluster of events that locate well ahead of the face correspond to events that occurred during the development of the setup room for Panel 2b.

Figure 9 shows a spatial count of events in the study area. There is increased seismicity near burst areas, but the most seismically active zones do not necessarily correspond to the locations of the bursts. Several of these areas of high seismicity occur in the vicinity of mapped faults, though it is difficult to say whether the faults are the sources of the events. A notable exception is the cluster of seismicity on the tailgate of Panel 4b that corresponded to mining of Panel 4b prior to Event 4.

Much like tectonic earthquakes, large seismic events in mines often exhibit well-defined aftershock sequences. The decay rate of the aftershocks is quantified by Omori's law [42] which describes the event count (n) as a function of time (t) and three constants ($c,\ k,\ p$) according to Eq. 3:

$$n\left(t\right)=\frac{k}{\left(c\ +\ t\right)^{p}} \tag{2}$$

The Omori parameters are useful in a post-burst context to help inform re-entry protocols (e.g., Vallejos and McKinnon [43]) and may provide some information about material stress and fracture maturity (e.g., Smirnov [44]). Most of the coal bursts, but especially Events 2, 3, and 4 exhibit a clear aftershock decay that is well described by the Unmodified Omori's Law ($p=1$, Fig. 10).

4.2 Load Transfer Distance and Numerical Modeling

Larson et al. [40] took the LTD determined from this dataset and added to it those determined from other NIOSH studies and those from the literature, for a total of 89 cases. They used reasonable sensitivity factor assumptions for other instrument types and ground condition surveys to adjust LTDs to an equivalent basis. Of the 89 cases, 33 had unknown stratigraphy. Two distinct LTD curves emerged from the 56 remaining cases. The discriminating factor to separate data points into two sets was whether there was an overburden member over 15 m (50 ft) thick—that is massive (at least one overburden member with thickness greater than or equal to 15 m) versus nonmassive (all overburden members having thickness less than 15 m). Both sets of data were fit to the same equation form as follows:

$$LTD_{nonmassive}=-64.27+253.1(1-exp(-0.004035H\,)) \tag{3}$$

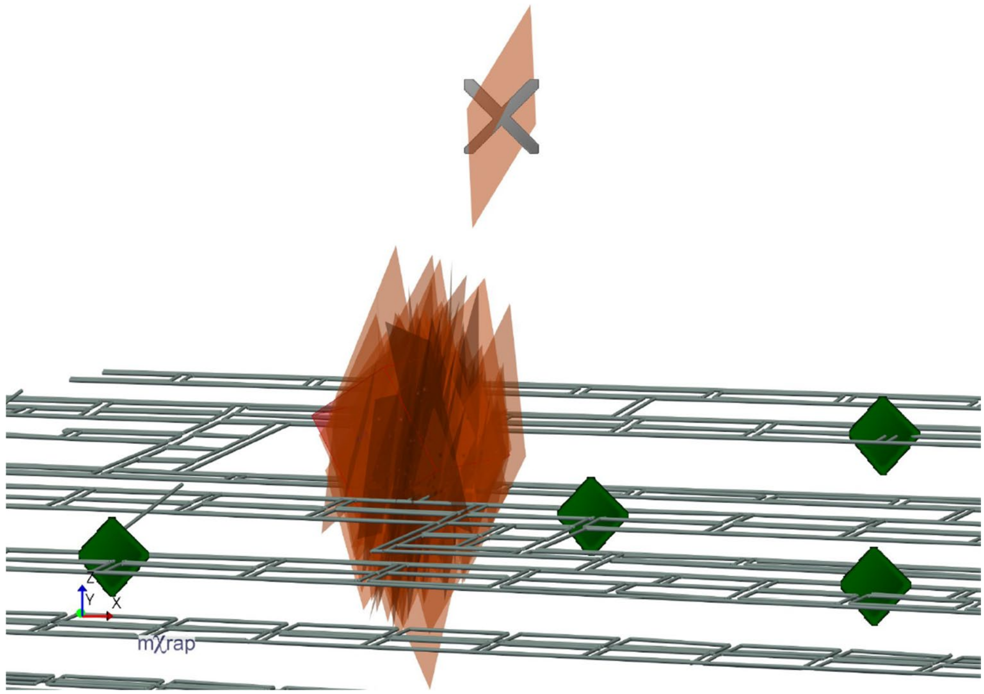

Fig. 7 Uncertainty planes for a small subset of events. The grey lines indicate the mine workings, green diamonds are the locations of seismic sensors, and the red rectangles indicate the plane of maximum location uncertainty (i.e., the least square approximation of the two largest axes of the 95% posterior point cloud)

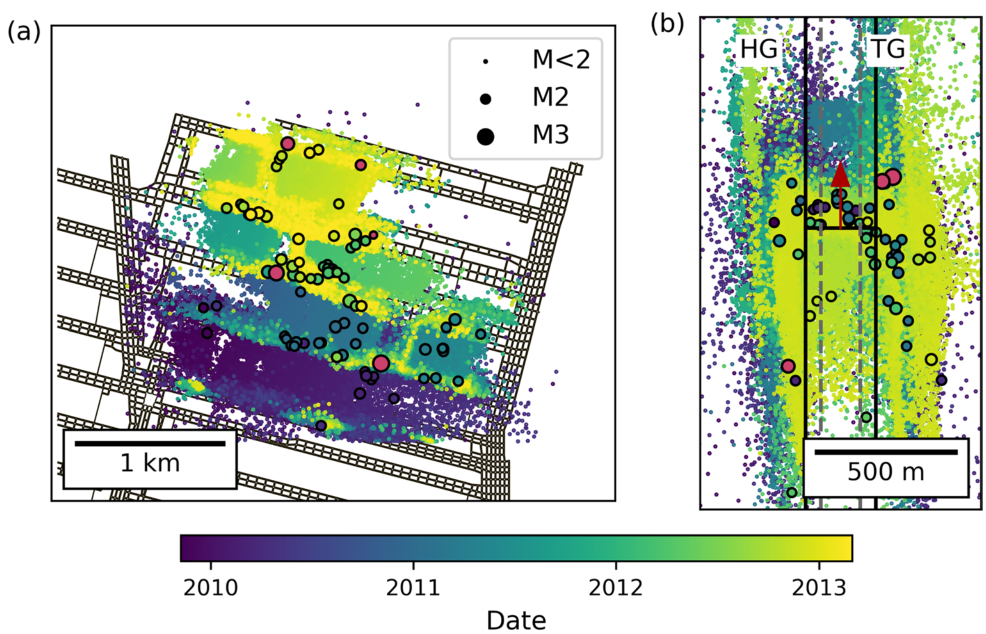

Fig. 8 Locations of the events in (**a**) plan view and (**b**) relative to the mining face at the time each event occurred (a face-centric coordinate system). Events are colored according to time. In (**b**), the horizontal black line indicates the location of the longwall face while the vertical lines indicate the width of the panel. The dotted grey lines indicate the reduced width of Panel 3b. The red arrow indicates the mining direction and the circles denote events with magnitude≥2 with pink circles indicating the locations of bursts. Not shown in (**b**): seismicity in the gateroads of previously mined panels, including Event 1

where H is overburden thickness, and $r^2=0.839$. For cases having an overburden member of 15 m thick, LTD was fit to the equation:

$$LTD_{massive} = -105.8 + 1186(1 - exp(-0.001158H)) \quad (4)$$

where $r^2 = 0.851$. The latter equation is stated incorrectly in Larson et al. [40], so these equations are corrected here. Eq. (3) was also fit using the same equation form as that used by Peng and Chiang [45] to be

$$LTD_{nonmassive} = 5.00\sqrt{H} \quad (5)$$

Although the r^2 of this equation was not as good ($r^2=0.539$) as it was for Eq. (3), the metric equivalent to the Peng and Chaing equation is

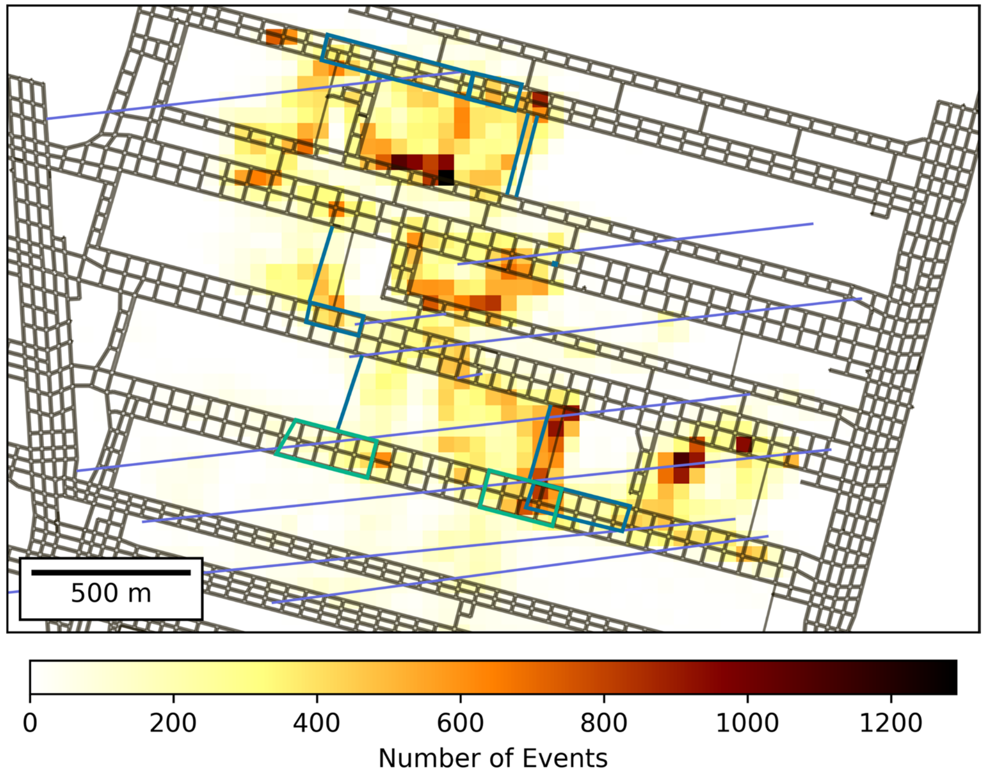

Fig. 9 Seismic event count binned spatially using 50-m by 50-m pixels. Grey lines show the mine workings and light purple lines represent faults. Blue lines and rectangles show the face positions and damage locations of the burst events, respectively. Green rectangles denote the anomalous zones observed in gateroad 2 N. Note that only four stations were operational during mining of Panel 1.

$$LTD = 5.13\sqrt{H} \quad (6)$$

which is nearly equivalent to Eq. (5). The fit to the same equation form for the data points that included a massive member, though not previously reported, was

$$LTD_{massive} = 19.1\sqrt{H} \quad (7)$$

where $r^2 = 0.694$. The ratio between the coefficients in the last two equations is 3.82. In other words, the equivalent LTD for environments with massive strata is nearly four times higher than those calculated using the empirical equation determined by the Peng and Chiang equation [22, 39].

Measured LTD was used to calibrate numerical models in FLAC3D, Mulsim, and LaModel. The details of achieving those calibrations are found in NIOSH [22]. Reasonable calibration was achieved with the former two models, but calibration with LaModel was only achieved when the overburden was so stiff that loading of the gob was negligible. The reason is that the overburden had to be very stiff to achieve the LTD because of the frictionless laminations formulation of LaModel.

Observations of floor heave and no floor heave were used to determine a range of strength properties of the floors of the gateroads [22, 46]. However, initial numerical models did not completely explain why floor heave occurred in some gateroads, and not in others [22]. Eventually, floor heave was associated with structural features [47]. The numerical modelling conducted with the Elk Creek dataset did not produce any useful information that pointed to improved gateroad design, because the models did not simulate the important structural features.

5 Event 2 Back Analysis

Event 2, the largest and first coal burst to damage multiple gate pillars during the study, offers a unique opportunity to conduct a back analysis of a coal burst because, in addition to the seismic data, ground deformation measurements and ground conditions surveys were performed in the vicinity of the event. The event occurred after mining approximately two-thirds of Panel 2 and damaged a 3-hectare area of the tailgate (2 N), registering as a magnitude 3.1. Several contributing factors are evidenced by the study data.

5.1 Geology and Caving Behavior

There are a couple of geologic structures of interest in the vicinity of the event. One of the anomalous zones in 2 N described in Sect. 2.1 overlaps the inby side of the damage zone from Event 2, and there is a fault that intersects the anomalous zone very close to the damaged area (Fig. 2). Additionally, some unusual caving conditions were observed

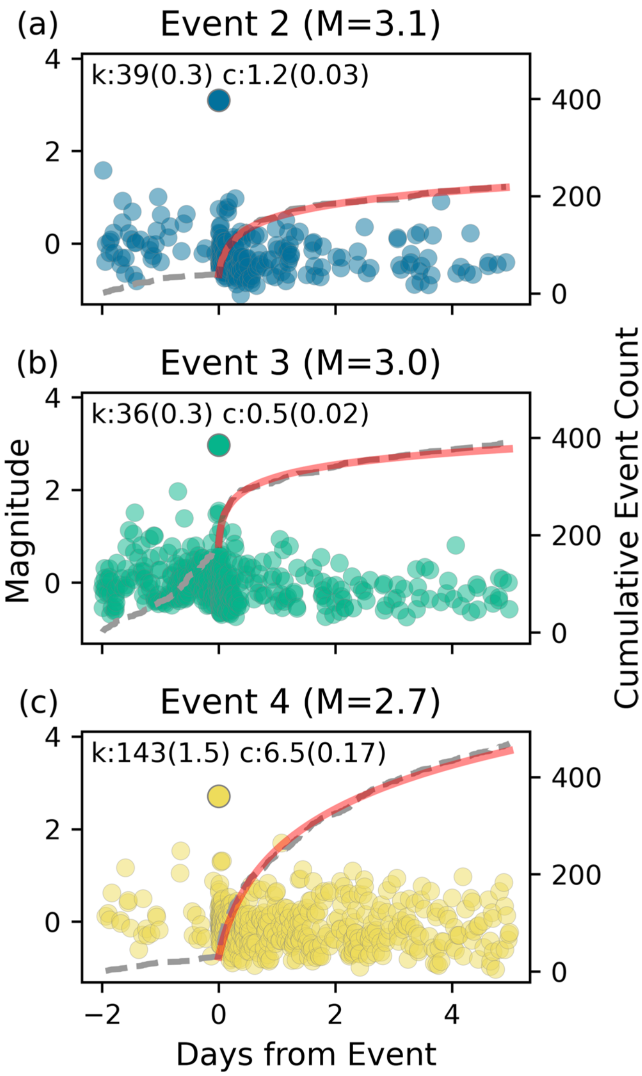

Fig. 10 Seismicity surrounding (**a**) Event 2, (**b**) Event 3, and (**c**) Event 4. Each dot represents a seismic event, the dotted gray line indicates cumulative event count, and the red line is the best fit Omori's Law with the parameters listed on the plot. Standard deviations of the fit parameters are in parentheses

when mining in Panel 1 in the vicinity of the burst area. Larson et al. [26] observed that gob formation in the first half of Panel 1 was gradual, but that caving occurred immediately behind the face. However, later into the panel—past the location of the area damaged by Event 2—Larson et al. observed that the behavior dramatically changed, and the roof stopped caving and instead sagged until it contacted the floor. This suggests a member in the immediate roof simply delaminated rather than breaking. Unfortunately, Larson et al. [26] did not observe where along the panel these conditions began.

Although the Event 2 occurred during the mining of Panel 2, the deterioration of the anomalous zone and change in caving behavior are both observable in the seismic data during mining of Panel 1. Figure 11 shows the progression of the seismicity as the longwall mined past the damage area of Event 2. The subplots each correspond to the same amount of face advance, except for the last subplot, which was extended slightly to include the face position when the lack of caving was observed underground. The amount of time that passed between subplots varies between 15 and 24 days. As the longwall approached the anomalous zone (Fig. 11a and b), the seismicity was distributed across the face in a typical manner. When the longwall reached the anomalous zone (Fig. 11b), there was a substantial uptick in the seismicity across the face, as well as an increase in seismicity in gateroad 2 N, particularly within the anomalous zone. Larson et al. [26] indicated that under normal conditions in 2 N the roof remained relatively intact while there was significant floor heave, whereas the anomalous zone also saw significant deterioration in the roof (Fig. 3). Therefore, the difference in seismicity in the anomalous area may be due to progressive roof failure. As mining progressed further into the anomalous zone (Fig. 11c), the seismicity largely shifted ahead of the face, with the highest concentration of seismicity occurring in the future damage area of Event 2. As the longwall continued to mine past the future damage area (Fig. 11d), there was very little seismicity at the face and in 1 N. The seismicity that did occur remained concentrated ahead of the face in 2 N. Finally, after mining passed the future damage zone (Fig. 11e), the seismicity in the panel largely dropped off. The lack of caving of the segment of Panel 1 near the damage area for Event 2 may have resulted in stress transfer onto the already deteriorating anomalous zone, priming the area for a future large burst. In this case, the dearth of seismic activity, in conjunction with abnormal caving conditions, indicated a latent coal burst hazard.

Changes in the seismicity are similarly observed when the face enters the anomalous zone during the mining of Panel 2, as shown in Fig. 12. In the month prior to Event 2, most of the seismicity locates in the headgate of the panel, which would be consistent with the pillars in the headgate taking load as the adjacent coal is extracted. After advancing approximately 55 m into the anomalous zone, a substantial increase in seismicity occurred across the face and onto the tailgate corner in addition to the seismicity on the headgate. This could be due to a possible increase in load transfer ahead of the face. Such a scenario might have taken place, for example, if the pillars in the anomalous zone began to yield. The over-panel weight would then be transferred mostly ahead of the face, potentially exacerbated by a roof member that did not fully cave during mining of the previous panel. The tailgate pillars, having less confinement than the panel, may have burst in response.

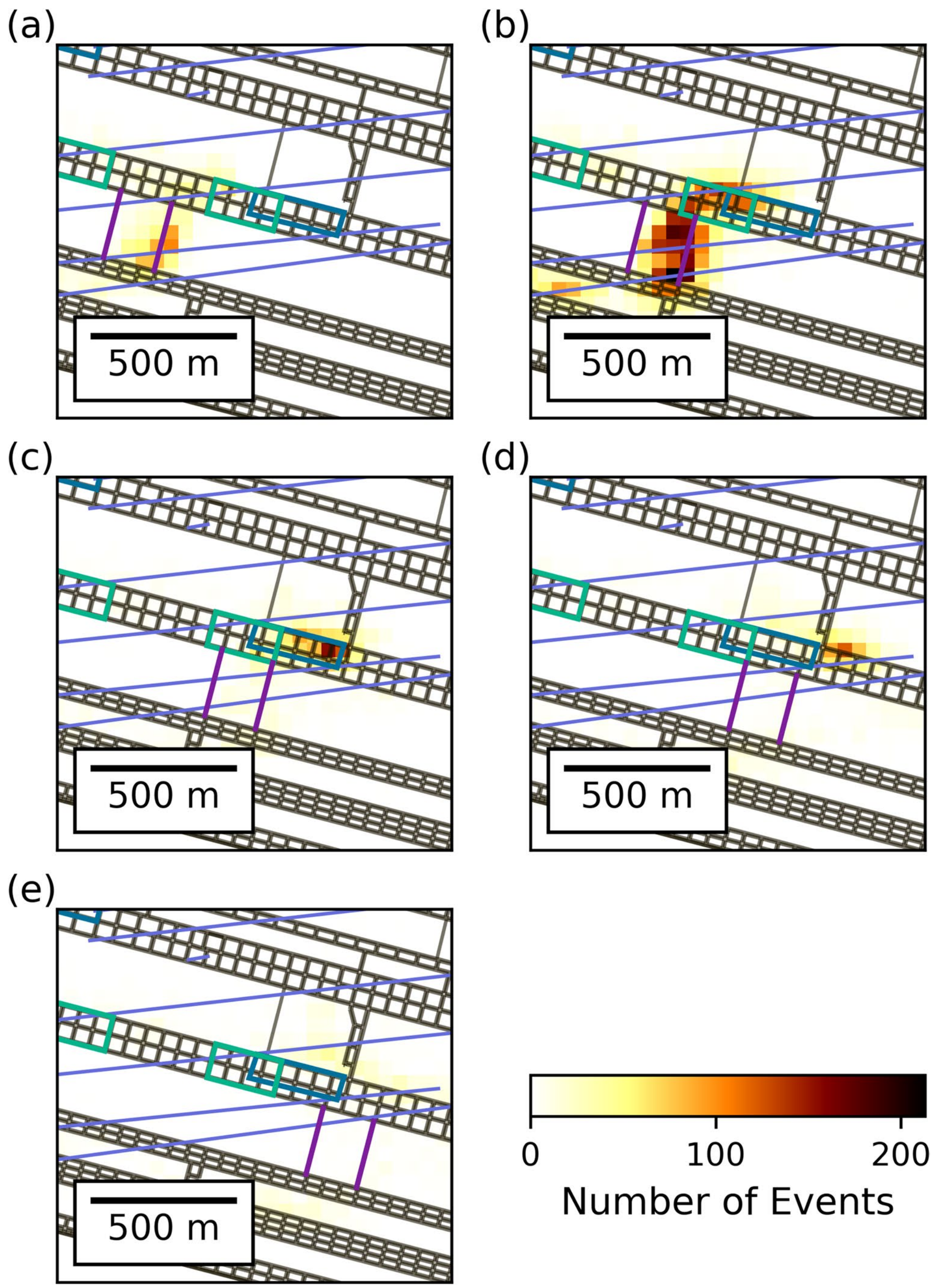

Fig. 11 Density plot of number of events during mining of Panel 1 as the longwall passed the area damaged during Event 2 (blue rectangle). Each subplot contains the seismicity that happened during mining of the area bounded by the purple lines. The anomalous zones are shown in light green and the faults are light purple

5.2 Moment Tensor Solution

Estimating moment tensors for coal mine seismicity is difficult due to the complex, time-varying, and anisotropic environment in which the events occur [48]. However, moment tensors can provide important insight into nature of the event. A moment tensor of Event 2 was determined using the Bayesian framework, Grond [49]. Two targets (goodness of fit metrics used in the inversion) were selected. First, the cross-correlation coefficient between manually selected phases filtered between 5 and 15 Hz and synthetic waveforms generated with a homogenous velocity model. Using cross correlation rather than an absolute comparison partially compensates for travel time errors and unmodeled velocity anisotropy. The second target was the manually picked polarity of the P-wave arrivals, again filtered between 5 and 15 Hz. The moment tensor solution is presented in Fig. 13. Because the closure of mine workings often dominates the low-frequency displacement field [50], damaging events frequently have significant implosive components, as was

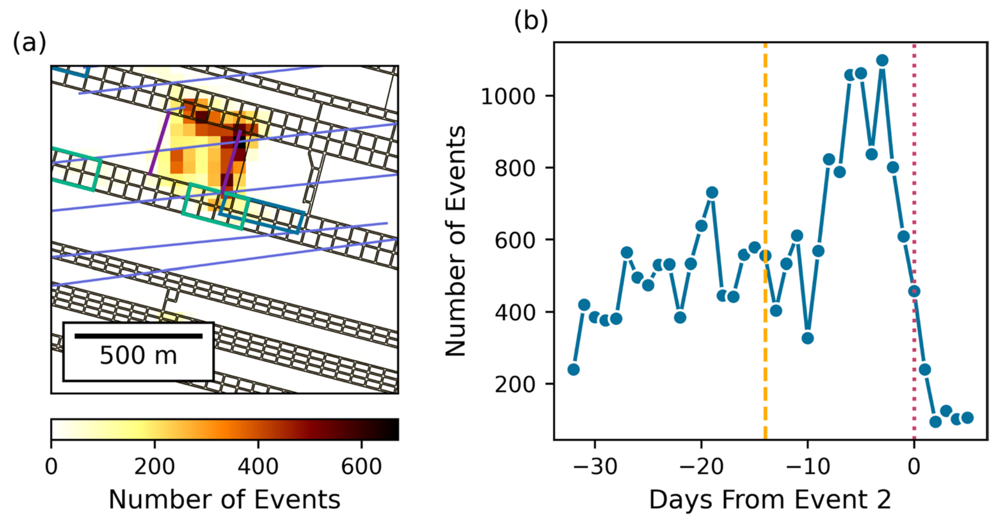

Fig. 12 Seismicity in the month leading up to Event 2. (**a**) shows the spatial count of events between January 17, 2011, and February 17, 2011 at 15:00 local time. (**b**) shows the number of events per day leading up to and shortly following Event 2. The dashed orange line indicates where the longwall face reached the anomalous zone and the dotted pink line indicates when Event 2 occurred.

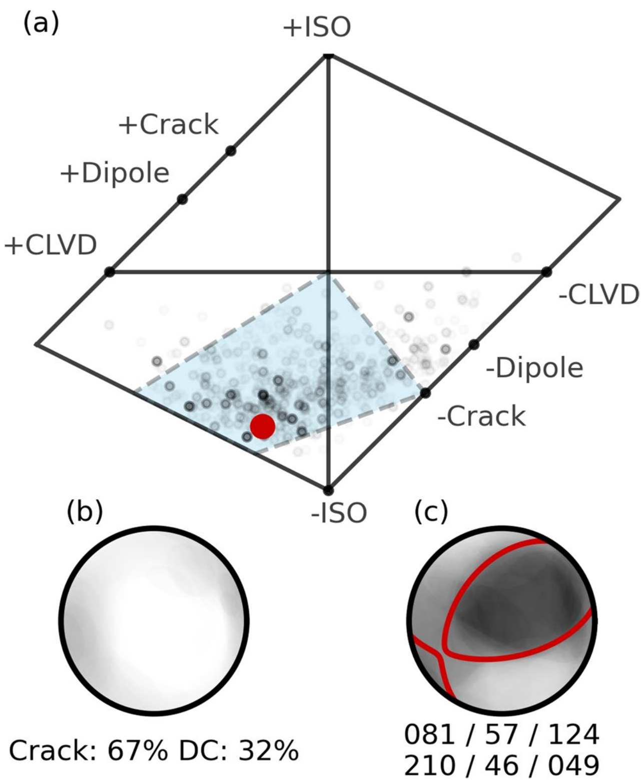

Fig. 13 Moment tensor solution of Event 2. Panel (**a**) shows a Hudson plot of the best solution (red dot) with other ensemble solutions plotted as gray dots. The region in which the CDC decomposition is valid shown as a blue patch. Panel (**b**) shows the ensemble total moment tensor slolutions with its closing crack and double couple ratios indicated. Panel (**c**) shows the ensemble DC solutions after removing the crack closing component, with the best fitting solution in red with the strike, dip, and rake of the focal planes listed below it

the case for Event 2 (Fig. 13a). The physically motivated Crack Double Couple (CDC) moment tensor decomposition [51] can separate the "crack closing" (e.g., convergence of workings) from the double couple (shear) moment tensor components. This was done for Event 2, assuming the crack closing direction (its P axis) was perpendicular to the coal seam (Fig. 13b and c).

The resulting moment tensor indicates most of the displacement field was caused by the closing of the workings, with a minor double couple (shear) component. While there is some scatter among the ensemble solutions, they primarily fall in the CDC region of the Hudson plot (Fig. 13a). One of the focal planes is oriented roughly at the same strike as the known fault system and indicates oblique reverse faulting. This is consistent with roof and floor convergence in the damaged area and shearing of the fault that crosses the anomalous zone, possibly affecting an un-caved roof member encountered during the mining of Panel 1. The post-event observation of significant entry convergence with most of the movement coming from the floor and ribs corroborate the moment tensor solution.

5.3 Instrumentation Response

The proximity of the underground instrumentation to Event 2 and its associated damage (Fig. 14) provides the ability to observe the loading and displacement caused by the burst near the damage zone. BPCs installed in Panel 2 and instruments in two sub-sites of site D (d1 and d2 in Fig. 14) are particularly useful in this regard. Site d1 had four instrumented Cans and two roof-to-floor string potentiometers, and site d2 had six instrumented Cans and four roof-to-floor potentiometers (see Fig. 19 in Larson et al. [26]). The Cans were also instrumented with string potentiometers, but these laregely measured the convergence of the Cans and the timber on top of the Cans rather than the movement in the workings. The loads on support Cans at site d2 were

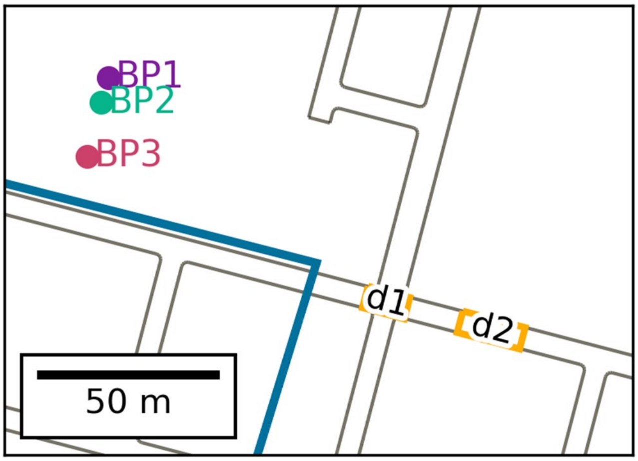

Fig. 14 Zoomed-in view of instrument site D showing the instrumented support Can sub-sites (d1 and d2) and the borehole pressure cells (labeled dots). The damage zone of Event 2 is shown in blue

monitored by a separate datalogger than the loads on Cans d1. The recording times for the d2 Cans were shifted so that the response to Event 2 lines up with that of the other instruments. The approximate 18-hour offset in the readings is likely due to the datalogger clock being set incorrectly after a battery change.

Figure 15 shows the response of the barrier pillar BPCs, the change in load on instrumented support Cans, and the convergence of the support Cans and roof-to-floor stations before and after Event 2, averaged for each sub-site. The BPCs show a gradual increase before the event as the longwall approaches, then a sudden increase in stress between 2.2 and 4.2 MPa during and after the event. A similar pattern is noted in the support Can load averaged by sub-site, and the averaged Can and roof-to-floor displacements. The increased load observed on both the BPCs and the support Cans and convergence are likely due to load transfer from the damaged zone to surrounding areas. The increased load in the barrier pillar is likely due to stress being transferred from the pillars destroyed by the event. Although the bulk of the load and convergence changes occur directly after Event 2, roughly two days passed before the system stabilized, approximately the duration of the aftershock sequence (Fig. 15b and c). Interestingly, while there is a clear response to the main burst, the subsequent spikes do not appear to coincide with any larger-magnitude aftershocks and are likely more related to smaller events occurring closer to the instrumentation. It is possible that the responses from this type of instrumentation could be used in conjunction with Omori's law to improve the assessment of re-entry time following significant events. Unfortunately, the roof-to-floor potentiometers at sub-site d1 were damaged during the event and thus did not produce usable data.

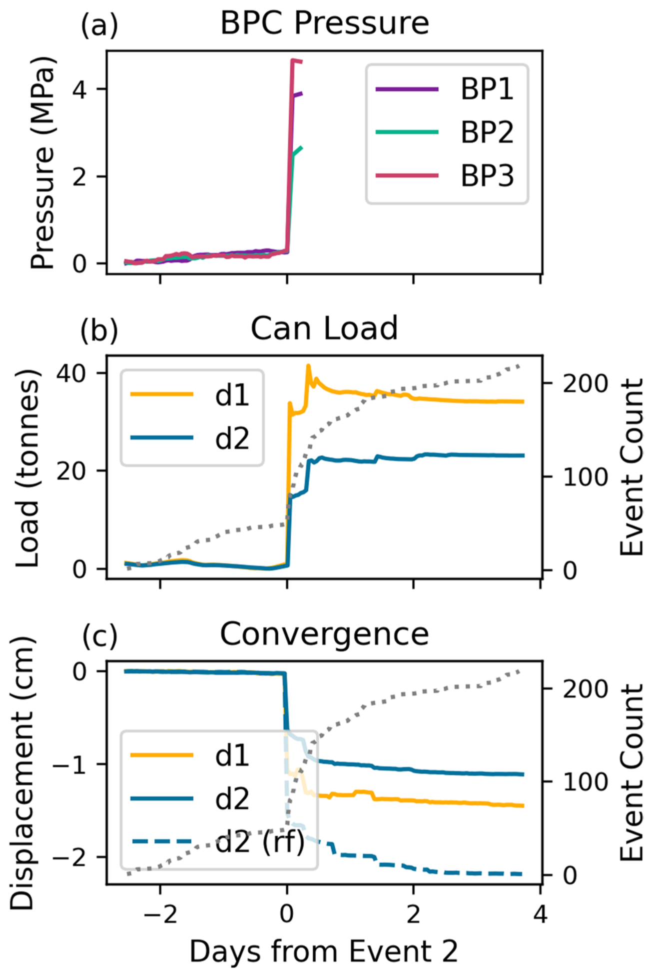

Fig. 15 Instrumentation response to Event 2 at instrumention site D. (**a**) shows the BPC response, (**b**) shows the support can load averaged by sub-site, and (**c**) shows the average Can displacement and roof-to-floor (rf) convergence again averaged by sub-site. The dotted grey line on panels (**b**) and (**c**) shows the cumulative event count in the area surrounding Event 2. In each case, the pre-burst measurements were subtracted from the absolute response to highlight the effect of the event

6 Discussion

6.1 Interpretation Considerations for the Seismic and Instrumentation Data

The use of in-mine microseismic systems is common practice for nearly all seismically active hard rock mines, but not for seismically active coal mines, especially in the US. Reasons for this lack of adoption ranges from prohibitive costs to sensor placement limitations. Swanson et al. [52] discuss these challenges and various monitoring strategies based on mine-specific needs. The use of in-mine sensors enables near-event recordings and can both improve the sensitivity of the seismic network and reduce location error uncertainties. However, this study also highlights some of the practical challenges of using in-mine stations, such as the need to constantly relocate sensors to maintain good coverage of the longwall face. Additionally, due to how the data were saved, the underground stations were only usable for a small percentage of the events because the P-wave arrivals were cut off, as described in Sect. 3.1. This could be mitigated in future by saving the continuous waveforms or at least longer event windows.

There are some important considerations when interpreting the seismic data for this dataset, particularly because the finalized events come from two different sources: the original catalog produced using JMTS and the catalog of events reprocessed with BEMIS. In particular, the methods used to calculate the source parameters for each catalog are different. Additionally, most of the events contributed by the original catalog occurred during the mining of Panel 1, when the network only consisted of four sites. As a result, in addition to the reduced sensitivity of the JMTS event detection compared to the BEMIS event detection, a significant amount of seismicity was likely outright missed from Panel 1. The reduced station coverage also makes the source parameters more sensitive to outliers. As such, the source parameters and event counts for Panel 1 should not be directly compared to those of the later panels. This is similarly true for the seven-hour gap in the BEMIS data from Panel 4, but it is a short enough time window that it is not expected to have a significant impact on interpretation. Similarly, the seismic sensors, especially those located in the mine, were frequently relocated during the study. The network reconfiguration was essential to maintain adequate seismic coverage of the mining face, but it resulted in changes to the sensitivity of the system over time that were largely ignored here.

Data reduction of BPCs using both the Lu method [34] or the Babcock method [35], with the assumptions and methods described by Vandergrift and Conover [36] resulted in calculations of compressive stress increase that were unreasonably high. To investigate this, Larson and Kim [37] conducted a numerical model study using FLAC to compare the behavior of BPCs under different ground conditions against a one-to-one increase in pressure with increasing applied stress. In their models they presented six cases, including elastic ground and under perfectly plastic behavior with increasing degrees of softening. They found that the BPC pressure overestimated the magnitude of the stress change compared to the elastic case with decreasing post-peak-strength of the stress-strain curve. The behavior observed at the Elk Creek mine was clearly not elastic, as seen by the estimated stresses and abutment loading. Furthermore, the coal at the mine is similar in nature to coals in Utah, which are found to exhibit brittle behavior [53]. As a result, the magnitude of the stresses recorded by the BPCs are likely overestimated. However, the sensitivity of the BPCs to changes in stress and the detection of increasing load is consistent.

6.2 Future Research Potential for the Elk Creek Dataset

The Elk Creek dataset has immense research potential beyond that presented in this study. This section highlights a few potential avenues for future research.

First, during the mining of Panel 4, the workers were withdrawn from the mine on January 8th, 2013, due to elevated levels of carbon monoxide caused by a thermal event. A few days later, workers were allowed to re-enter the mine but were evacuated again due to gas levels. The mine was subsequently sealed and decommissioned. Although the in-mine sensors went offline on January 9th, 2013, the surface stations continued for several months after the mine closure. These data are potentially useful for tracking the progress of the underground fire and studying mine relaxation.

Although some important observations were made about the seismicity surrounding Event 2, additional work could be conducted to examine conditions surrounding the other events. Quantifying and back analysing seismic risk using the same framework commonly used in hard rock mines (e.g., Hudyma and Potvin [54] and Wesseloo [55]) could be particularly insightful as rigorous seismic hazard analysis is not commonly conducted in coal mines.

As mentioned previously, moment tensor inversion for coal mine events is very difficult due to the complex, anisotropic, time-varying medium in which the events occur. Although the simplistic approach taken in this work yielded some insights, this dataset offers the opportunity for improvement. For example, heterogenous, anisotropic models could be used to generate more realistic Green's functions for the inversion. Moreover, unlike most tectonic earthquakes, the coal bursts reported here certainly contain some net mass movement, so a joint moment tensor, force system may be required to adequately describe the displacement field. Expanding the inversion approach to also include single forces may better fit the data.

The geotechnical instrumentation was used to assess load transfer distance and quantify the mine's reaction to Event 2, but it could be used for additional purposes. For example, exploring the relationship between pressure and displacement to track the coal pillar transition from elastic to plastic behavior, searching for coal burst precursors, better quantifying the response to small seismic events, and using the measured displacements to help constrain the moment tensor inversion could all be fruitful avenues.

7 Conclusions

This paper presents a case study of a “close-in” seismic array with both in mine and surface stations to monitoring mining-induced seismicity at an underground coal mine. While the inclusion of in-mine stations has the potential to improve event location accuracy, they could only be used for a small percentage of the events due to short duration event recording windows. In future studies, it would be preferable to save a longer window of data ahead of the arrival or, ideally, to save the entire continuous archive which is more practical today with modern hard drives and cloud storage.

The use of an automated, Bayesian code for the picking, location, and source parameters resulted in more consistent results with a higher precision than was previously observed. As a result, more detail is available about how the seismic events locate in relation to the mine workings and other structures. Events with location residuals less than 80 m show that most of the seismicity locates near the mining face with some residual seismicity in the gateroads and in the previously mined areas. The seismicity largely concentrates near mapped faults, suggesting geological structure plays an important role in variations of seismicity and the observed coal bursts. LTDs at this mine were also found to be abnormally high, likely due to the presence of strong, competent sandstone units in near seam geology, which likely contributed to the mine’s propensity to burst.

Event 2, the largest coal burst observed during the study window, was preceded by unusual behavior noted during mining of the previous panel. Specifically, abnormal caving and the migration of seismicity to the headgate ahead of the face, which corresponded to a geologically anomalous zone and fault intersection and overlapped with the damage area of the event. The lack of seismicity observed during the mining of Panel 1, especially in conjunction with the observation that the immediate roof stopped caving, foreshadowed a latent seismic hazard. While it is always easier to identify such indicators after the fact, this instance serves as an important reminder that when there is a significant change in the mine’s seismic response it is prudent to evaluate conditions and ensure the geomechanics are understood. Moment tensor inversion of the coal burst indicates convergence of the mine workings with minor movement along a structure roughly consistent with the intersecting fault. While not examined in this paper, it would be interesting to do similar back analyses for the other large bursts, in particular exploring the relationship between the sandstone channel in Panel 4 and the seismicity observed in that area.

The seismicity following the major coal bursts is well described by Omori’s law. Similarly, the loading and convergence of the support Cans monitoring at instrumentation site D continued to show spikes over a similar time window as the aftershock sequence for Event 2. This information could be useful for evaluating the aftershock sequence and determining when it is safe to re-enter the area following a large burst.

Finally, the Elk Creek dataset, which is being released alongside this study, holds significant potential for future research.

Acknowledgements The authors are extremely grateful for the collaboration from Elk Creek mine personnel, and for their willingness to allow the release of this important case study and the associated data to advance mine safety research. We also acknowledge several retired NIOSH researchers who played pivotal roles in making this research possible. Specifically, we acknowledge the contributions of the following individuals: Peter Swanson, Eric Zahl, Richard Rains, Jerry Richardson, Steve Ward, Steve Iverson, Curtis Clark, Michael Stepan, Brad Seymour, and Jeff Whyatt, all affiliated or formerly affiliated with NIOSH Spokane Research Laboratory; Craig Compton, Dennis Dolinar, David Oyler, Tristan H. Jones, David Gearhart, and Tim Batchler, all affiliated or formerly affiliated with NIOSH Pittsburgh Research Laboratory; and Doug Smith, Mike Ludlow, and Justin Evans, all affiliated or formerly with Oxbow Mining, Inc. Also, personnel from Agapito and Associates, who designed part of the instrumentation plan that includes the BPCs and MPBX extensometers and drilled BPC boreholes for and installed those instruments.

Data Availability The Elk Creek dataset and the code to reproduce most of the figures can in this paper be found at www.github.com/niosh-mining/elkcreek. The following software packages were used in this research: ObsPy [56], ObsPlus [57], Pyrocko [58], and mXrap [59].

Declarations

The findings and conclusions in this paper are those of the authors and do not necessarily represent the official position of the National Institute for Occupational Safety and Health, Centers for Disease Control and Prevention or any other affiliated organization of the authors.

Competing interests The authors have no competing interests to declare that are relevant to the content of this article.

References

1. Zhang C, Canbulat I, Hebblewhite B, Ward CR (2017) Assessing coal burst phenomena in mining and insights into directions for future research. Int J Coal Geol 179:28–44. https://doi.org/10.1016/j.coal.2017.05.011
2. Kidybinski A (2011) The effect of porosity and the strength of coal on the dynamics of coal and methane outburst–The Bpm modelling. Arch Min Sci 56(3):415–426. https://www.researchg

ate.net/publication/298421225_The_effect_of_porosity_and_the_strength_of_coal_on_the_dynamics_of_coal_and_methane_outburst_-_The_bpm_modelling
3. MSHA (2020) Mine data retrieval system, Mine Safety and Health Administration (MSHA), U.S. Department of Labor. https://www.msha.gov/data-and-reports/mine-data-retrieval-system
4. Rong H, Li N, Zhang H, Sun D, Huo B (2022) Insights into fundamental problems of rockburst under the modern structure stress field. Sci Rep 12(1):1–11. https://doi.org/10.1038/s41598-022-24857-4
5. Mutke GZ, Dubiński J, Lurka AI (2015) New criteria to assess seismic and rock burst hazard in coal mines. Arch Min Sci 60(3):743–760. https://doi.org/10.1515/amsc-2015-0049
6. Lama RD, Bodziony J (1998) Management of outburst in underground coal mines. Int J Coal Geol 35(1–4):83–115. https://doi.org/10.1016/S0166-5162(97)00037-2
7. Rice GS (1936) Bumps in coal mines—theories of causes and suggested means of prevention or of minimizing effects. Trans Am Inst Min Metall Eng 119:11–39. https://onemine.org/documents/underground-mining-bumps-in-coal-mines-theories-of-causes-and-suggested-means-of-prevention-or-of-minimizing-effects-with-discussion-
8. Iannacchione AT, Tadolini SC (2016) Occurrence, predication, and control of coal burst events in the U.S. Int J Min Sci Tech 26(1):39–46. https://doi.org/10.1016/j.ijmst.2015.11.008
9. Vardar O, Zhang C, Canbulat I, Hebblewhite B (2018) A semi-quantitative coal burst risk classification system. Int J Min Sci Tech. https://doi.org/10.1016/j.ijmst.2018.08.001
10. Frith R, Reed G, Mackinnon M (2020) A discussion on causation mechanisms for overburden bumps as distinct from coal bursts. In: Aziz N, Kininmonth B, (eds) Proceedings of the 2020 Coal Operators' Conference, February 18–20, 2019: University of Wollongong. pp. 219–32. https://ro.uow.edu.au/coal/775
11. Mark C (2016) Coal bursts in the deep Longwall mines of the united States. Int J Coal Sci Tech 3(1):1–9. https://doi.org/10.1007/s40789-016-0102-9
12. Pechmann JC, Arabasz WJ, Pankow KL, Burlacu R, McCarter MK (2008) Seismological report on the 6 August 2007 Crandall Canyon mine collapse in Utah. Seis Res Lett 79(5):620–636. https://doi.org/10.1785/gssrl.79.5.620
13. MSHA (2008) Report of investigation—Fatal underground coal burst accidents, August 6 and 16, 2007, Crandall Canyon Mine, Genwal resources Inc, Huntington, Emery County, Utah, CAI-2007-15-17, 19–24. 472 pp
14. Ellenberger JL, Heasley KA, Swanson PL, Mercier J (2001) Three dimensional microseismic monitoring of a Utah longwall. Rock Mechanics in the National Interest: Proceedings of the 38th Rock Mechanics Symposium. 38th Rock Mechanics Symposium, DC Rocks, 2001, July 7–10, 2001, Washington, DC: A. A. Balkema. pp. 1321–6. https://onepetro.org/ARMAUSRMS/proceedings-abstract/ARMA01/ARMA01/ARMA-01-1321/117560
15. Mark C, Gauna M (2021) Pillar design and coal burst experience in Utah book cliffs Longwall operations. Int J Min Sci Tech 31(1):33–41. https://doi.org/10.1016/j.ijmst.2020.12.008
16. Kissell FN, Iannacchione AT (2014) Gas outbursts in coal seams. In: Thakur P, Schatzel S, Aminian K (eds) Coal bed methane: from prospect to pipeline. Elsevier, Waltham, MA, pp 177–184
17. Mark C (2018) Coal bursts that occur during development: A rock mechanics enigma. Int J Min Sci Tech 28(1):35–42. https://doi.org/10.1016/j.ijmst.2017.11.014
18. Swanson P, Stewart C, Koontz W (2008) Monitoring coal mine seismicity with an automated wireless digital strong motion network. In: Peng SS, Mark C, Finfinger G, Tadolini S, Khair AW, Heasley K, (eds) Proceedings: 27th International Conference on Ground Control in Mining, July 29–31, 2008, Morgantown, WV: West Virginia University. pp. 79–86. https://www.onetunnel.org/documents/monitoring-coal-mine-seismicity-with-an-automated-wireless-digital-strong-motion-network
19. Carroll CJ (2003) Fractures in the Mesaverde group at Somerset coal Field, delta and Gunnison Counties, Colorado. Piceance basin guidebook. Rocky Mountain Association of Geologists, Denver, CO, pp 194–207
20. Osmond JC (1964) Tectonic history of the Uinta Basin, Utah. In: Sabatka EF, (ed) Guidebook to the Geology and Mineral Resources of the Uinta Basin: Utah's Hydrocarbon Storehouse, Thirteenth Annual Field Conference, September 16–19, 1964, Salt Lake City, UT: Intermountain Association of Petroleum Geologists (IAPG). pp. 47–68. https://archives.datapages.com/data/uga/data/013/013001/47_ugs130047.htm
21. Schultz JE, Eakins W, Scott DC, Teeters DD (2000) Availability of coal resources in colorado: Somerset coal Field, West-Central Colorado. Denver CO 94. https://doi.org/10.58783/cgs.rs38.nkeo4105
22. NIOSH (2020) Ground stress in mining (part 2): calibrating and verifying Longwall stress models. Spokane WA Publication 2020–104 RI 9703:273pp. https://www.cdc.gov/niosh/docs/mining/works/coversheet2136.html
23. Agapito JFT, Gilbride L, Koontz W (2005) Implication of highly anisotropic horizontal stresses on entry stability at the West Elk Mine, Somerset, Colorado. In: Peng SS, Mark C, Finfinger GL, Tadolini SC, Heasley KA, Khair AW, (eds) Proceedings: 24th International Conference on Ground Control in Mining, August 2–4, 2005, Morgantown, WV: West Virginia University. pp. 196–202. https://www.agapito.com//wp-content/uploads/2010/04/Implication-of-Highly-Anisotropic-Horizontal-Stresses-on-Entry-Stability-at-the-West-Elk-Mine-Somerset-Colorado.pdf
24. USBM (1993) Rock stress determinations from overcoring—an overview. Pittsburgh, PA, Bulletin 694. 176 pp., https://ntrl.ntis.gov/NTRL/dashboard/searchResults/titleDetail/PB94108826.xhtml
25. Mark C, Phillipson S, Tyrna P, Gauna M (2012) Characteristics of coal bursts in the North Fork Valley of the Gunnison River Valley, Colorado. In: Barczak T, Tadolini S, Opfer D, Thompson M, Caudill D, Warnick B, (eds) Proceedings: 31st International Conference on Ground Control in Mining, July 31–August 2, 2012, Morgantown, WV: West Virginia University. pp. 1–13. https://onemine.org/documents/characteristics-of-coal-bursts-in-the-north-fork-valley-of-the-gunnison-river-valley-colorado
26. NIOSH (2020) Ground stress in mining (part 1): measurements and observations at two Western U.S. Longwall mines. Spokane WA Publication 2020–103 RI 9702:169pp. https://www.cdc.gov/niosh/docs/mining/works/coversheet2137.html
27. Lawson H, Zahl E, Whyatt J (2012) Ground condition mapping: A case study. Seattle, WA: Society for Mining, Metallurgy, and Exploration, Inc., 7 pp., https://www.researchgate.net/publication/308765486_Ground_Condition_Mapping_A_Case_Study
28. Törnman W, Martinsson J (2020) Reliable automatic processing of seismic events: solving the Swiss cheese problem. In: Wesseloo J, (ed) UMT 2020: Proceedings of the Second International Conference on Underground Mining Technology, November 3–4, 2020, Perth: Australian Centre for Geomechanics. pp. 155–72. https://doi.org/10.36487/ACG_repo/2035_04
29. King A (2012) Velocity model determination for accurate location of mining-induced seismic events. Proceedings of the 22nd International Geophysical Conference and Exhibition, February 26–29, 2012, Brisbane, Australia: Australian Society of Exploration Geophysicists (ASEG). pp. 1–4. https://doi.org/10.1071/ASEG2012ab126
30. Törnman W, Martinsson J, Svanberg E (2024) Enriching seismic data with noise and blasts and the importance of credibility. Proceedings of the 10th International Conference on Deep and High Stress Mining. Deep Mining 2024, September 24–26, 2024, Montréal, Canada: Australian Centre for Geomechanics. pp. 207–16. https://doi.org/10.36487/ACG_repo/2465_08
31. Törnman W, Martinsson J, Dineva S (2021) Robust bayesian estimator for S-wave spectra, using a combined empirical green's function. Geophys J Int 227:403–438. https://doi.org/10.1093/gji/ggab184

32. Brune JN (1970) Tectonic stress and the spectra of seismic shear waves from earthquakes. J Geophys Res 75(26):4997–5009. https://doi.org/10.1029/JB075i026p04997
33. Larson MK MulsimNL/Large: Reviving a USBM tool for modeling coal mines. Denver, CO: Society for Mining Metallurgy, and, Exploration (2015) Inc., 11 pp., https://onetunnel.org/documents/mulsimnl-large-reviving-a-usbm-tool-for-modeling-coal-mines
34. Lu PH (1984) Mining-induced stress measurement with hydraulic borehole pressure cells. In: Dowding CH, Singh MM, (eds) Rock Mechanics in Productivity and Protection, Proceedings: Twenty-Fifth Symposium on Rock Mechanics, June 25–27, 1984, Evanston, IL: Society of Mining Engineers. pp. 204–11. https://onepetro.org/ARMAUSRMS/proceedings-abstract/ARMA84/ARMA84/ARMA-84-0204/131235
35. Babcock CO (1986) Equations for the analysis of borehole pressure cell data. In: Hartman HL, (ed) Rock Mechanics: Key to Energy Production, Proceedings of the 27th US Symposium on Rock Mechanics, June 23–25, 1986, Tuscaloosa, AL: Society of Mining Engineers. pp. 233–40. https://www.onetunnel.org/documents/equations-for-the-analysis-of-borehole-pressure-cell-data
36. Vandergrift T, Conover D (2010) Assessment of gate road loading under deep western U.S. conditions. In: Mark C, Barczak T, Esterhuizen GS, (eds) Proceedings: 3rd International Conference on Coal Pillar Mechanics and Design, July 26, 2010, Morgantown, WV: West Virginia University. pp. 38–46. https://www.agapito.com/portfolio-posts/assessment-of-gate-road-loading-under-deep-western-u-s-conditions/
37. Larson MK, Kim B-H (2019) Performance analysis of instruments used to measure stress change resulting from mining. In: Klemetti T, Mishra B, Lawson H, Murphy M, Perry K, (eds) Proceedings of the 38th International Conference on Ground Control in Mining, July 23–25, 2019, Morgantown, WV: Society for Mining, Metallurgy, and Exploration, Inc. (SME). pp. 301–10. https://www.researchgate.net/publication/334812262_Performance_Analysis_of_Instruments_Used_to_Measure_Stress_Change_Resulting_from_Mining
38. Heasley KA (2008) Some thoughts on calibrating LaModel. In: Peng SS, Mark C, Finfinger G, Tadolini S, Khair AW, Heasley KA, (eds) Proceedings: 27th International Conference on Ground Control in Mining, July 29–31, 2008, Morgantown, WV: West Virginia University. pp. 7–13
39. Larson MK, Whyatt JK (2012) Load transfer distance calibration of a coal panel scale model: A case study. In: Barczak T, Tadolini S, Opfer D, Thompson M, Caudill D, Warnick B, (eds) Proceedings of the 31st International Conference on Ground Control in Mining, July 31–August 2, 2012, Morgantown, WV: West Virginia University. pp. 195–205. https://onemine.org/documents/load-transfer-distance-calibration-of-a-coal-panel-scale-model-a-case-study
40. Larson MK, Lawson HE, Tesarik DR (2015) Load transfer distance measurements at two mines in the western U.S. In: Barczak TM, Tadolini S, Heasley K, (eds) Proceedings of the 34th International Conference on Ground Control in Mining, July 28–30, 2015, Morgantown: West Virginia University. pp. 54–64. https://www.onemine.org/documents/load-transfer-distance-measurements-at-two-mines-in-the-western-u-s-
41. Boltz MS, Chambers DJA, Hanson DR (2018) Evaluating seismicity at underground coal mines using temporary surface geophone deployments. Seattle, WA: American Rock Mechanics Association (ARMA). https://onepetro.org/ARMAUSRMS/proceedings-abstract/ARMA18/ARMA18/ARMA-2018-493/122457
42. Guglielmi AV (2017) Omori's law: a note on the history of geophysics. Physics—Uspekhi 60(3):319–324. https://doi.org/10.3367/UFNe.2017.01.038039
43. Vallejos JA, McKinnon SD (2011) Correlations between mining and seismicity for re-entry protocol development. Int J Rock Mech Min Sci 48(4):616–625. https://doi.org/10.1016/j.ijrmms.2011.02.014
44. Smirnov VB, Ponomarev AV, Stanchits SA, Potanina MG, Patonin AV, Dresen G et al (2019) Laboratory modeling of aftershock sequences: stress dependences of the Omori and Gutenberg-Richter parameters. Izv Phys Solid Earth 55:124–137. https://doi.org/10.1134/S1069351319010105
45. Peng SS, Chiang HS (1984) Longwall mining. Wiley, New York
46. Tesarik DR, Whyatt JK, Larson MK (2013) Inferring mine floor properties from pillar size and floor heave. In: Pyrak-Nolte LJ, Alvin C, Dershowitz W, Morris J, Rostami J, (eds) Proceedings of the 47th US Rock Mechanics/Geomechanics Symposium, June 23–26, 2013, San Francisco, CA: American Rock Mechanics Association. pp. 438–50. https://www.researchgate.net/publication/275272673_Inferring_Mine_Floor_Properties_from_Pillar_Size_and_Floor_Heave
47. Kim BH, Larson MK (2022) Assessment of floor heave associated with bumps in a Longwall mine using the discrete element method. Min Metall Explor 39:1853–1861. https://doi.org/10.1007/s42461-022-00596-y
48. King AR (2005) Source-parameter estimation in a coal environment. In: Potvin Y, Hudyma M, (eds) Controlling Seismic Risk: Sixth International Symposium on Rockburst and Seismicity in Mines Proceedings, March 8–11, 2005, Perth, Australia: Australian Centre for Geomechanics. pp. 131–4. https://doi.org/10.36487/ACG_repo/574_8
49. Heimann S, Isken M, Kühn D, Sudhaus H, Steinberg A, Vasyura-Bathke H et al (2018) Grond – A probabilistic earthquake source inversion framework: GFZ Data Services. https://github.com/braunfuss/grond
50. Malovichko D (2020) Description of seismic sources in underground mines: theory. Bull Seis Soc Am 110(5):2124–2137. https://doi.org/10.1785/0120200093
51. Rigby A (2024) Physically motivated moment-tensor decomposition for mining-induced seismicity. Geophys J Int 236(1):443–455. https://doi.org/10.1093/gji/ggad430
52. NIOSH (2016) Seismic monitoring strategies for deep longwall coal mines. Spokane, WA. 100 pp., https://www.cdc.gov/niosh/docs/mining/works/coversheet1944.html
53. Kim B-H, Walton G, Larson MK, Berry S (2021) Investigation of the anisotropic confinement-dependent brittleness of a Utah coal. Int J Coal Sci Tech 8:274–290. https://doi.org/10.1007/s40789-020-00364-7
54. Hudyma M, Potvin YH (2010) An engineering approach to seismic risk management in hardrock mines. Rock Mech Rock Eng 43:891–906. https://doi.org/10.1007/s00603-009-0070-0
55. Wesseloo J (2018) The Spatial assessment of the current seismic hazard state for hard rock underground mines. Rock Mech Rock Eng 51(6):1839–1862. https://doi.org/10.1007/s00603-018-1430-4
56. Krischer L, Megies T, Barsch R, Beyreuther M, Lecocq T, Caudron C et al (2015) ObsPy: A Bridge for seismology into the scientific python ecosystem. Comp Sci Discov 8(1). https://doi.org/10.1088/1749-4699/8/1/014003
57. Chambers DJA, Boltz MS, Chamberlain CJ (2021) ObsPlus: A Pandas-centric obspy expansion pack. J Open Source Softw 6(60). https://doi.org/10.21105/joss.02696
58. Heimann S, Kriegerowski M, Isken M, Cesca S, Daout S, Grigoli F et al (2017) Pyrocko - An open-source seismology toolbox and library. GFZ Data Serv. https://doi.org/10.5880/GFZ.2.1.2017.001
59. Harris PC, Heinsen Egan M, Niedzielski LG, Cumming-Potvin D (2023) mXrap. Perth, Western Australia: Australian Centre for Geomechanics. https://mxrap.com